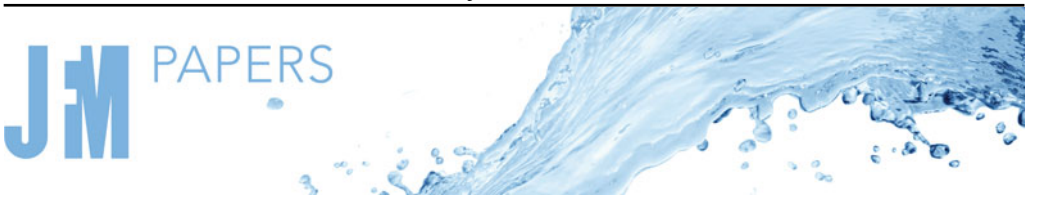
J. Fluid Mech. (2026), *vol.* 1030, A49, doi:10.1017/jfm.2026.11278



Thermodynamically admissible diffuse interface model for nanoscale transport of dense fluids

Rahul Bhattacharjee[1], **Henning Struchtrup**[2] **and Anirudh Singh Rana**[1]

[1]Department of Mathematics, Birla Institute of Technology and Science Pilani, Rajasthan 333031, India

[2]Department of Mechanical Engineering, University of Victoria, PO Box 1700 STN CSC, Victoria, V8W 2Y2, BC, Canada

Corresponding author: Anirudh Singh Rana, anirudh.rana@pilani.bits-pilani.ac.in

(Received 2 May 2025; revised 26 November 2025; accepted 2 February 2026)

We investigate the interfacial fluid dynamics and heat transfer at nanoscales using an improved diffuse interface approach for liquid–vapour interfaces in non-equilibrium. Conventional Navier–Stokes–Korteweg (NSK) formulations often fail to accurately capture transport phenomena across extremely thin interfaces due to underestimation of interface resistances. In this work, we improve the NSK model by adding a production term in the momentum equation based on higher-order corrections. To enhance interface resistances, viscosity and thermal conductivity are made dependent on the density gradient, increasing resistance only within the interface region. The gradient-based coefficients are determined by fitting to solutions of the Enskog–Vlasov equation for Couette flow of Struchtrup & Frezzotti (2022 *J. Fluid Mech.*, vol. 940, p. A40). Applying these fitted equations to pure heat conduction and planar evaporation problems shows that the model accurately captures interfacial transport, making it a useful tool for studying nanoscale evaporation, thermal management and the droplet dynamics on solid surfaces.

Key words: condensation/evaporation, Navier-Stokes equations, multiphase flow

1. Introduction

Nanoscale phase transition plays a vital role in modern thermal management systems, which are essential in applications ranging from high-performance electronics and energy systems to advanced manufacturing (Gong, Hu & Cheng 2024). Technologies such as heat pipes, microchannel evaporators, phase-change cooling and thin-film boiling devices rely heavily on accurate modelling of phase transition at liquid–vapour interfaces (Dupont, Thome & Jacobi 2004; Mukherjee 2009; Rana, Lockerby & Sprittles 2019; Taassob *et al.* 2021). As device sizes shrink and localised heat flux increases, predicting interfacial transport processes with high physical fidelity has become increasingly critical.

© The Author(s), 2026. Published by Cambridge University Press.

https://doi.org/10.1017/jfm.2026.11278 Published online by Cambridge University Press

Accurate modelling of such phenomena requires capturing the interplay between capillarity, surface forces and transport processes within the interfacial region – a challenge that spans from the microscale to the nanoscale (Anderson, McFadden & Wheeler 1998; Bhattacharjee *et al.* 2024*a*).

A popular theoretical framework for simulating such multiphase systems is provided by the Navier–Stokes–Korteweg (NSK) equations, which originated from the foundational ideas of Gibbs (1878) on the concept of a dividing surface, and were later extended through the thermodynamic formulation of diffuse interfaces by van der Waals (1979) and Korteweg (1901). These pioneering studies established that interfaces possess finite thickness, with van der Waals notably demonstrating how this thickness diverges near critical temperatures using his equation of state. Building upon these classical foundations, modern implementations of the NSK equations augment the classical Navier–Stokes system with a Korteweg stress to represent capillarity in a diffuse interface setting (Anderson *et al.* 1998). In this formulation, the interface is treated as a finite region across which fluid properties vary smoothly, rather than as a sharp boundary (Garcke & Novick-Cohen 2000). Recent advances in numerical methods have significantly enhanced NSK modelling capabilities: Gomez *et al.* (2010) employed isogeometric analysis, while Liu *et al.* (2013) developed a semi-discrete Galerkin method using functional entropy variables. Other notable contributions include Diehl *et al.* (2016), who employed a numerical approximation method on the basis of the local discontinuous Galerkin method, Martínez *et al.* (2020), who used a high-order finite volume method for phase-change simulations and Tian *et al.* (2016), who used a adaptive local discontinuous Galerkin method for non-isothermal flows. Contemporary work by Souček *et al.* (2020) on second-law-compliant boundary conditions and Dhaouadi & Dumbser (2023) on a structure-preserving finite volume scheme further demonstrate the ongoing development of this framework. Despite these advances, the standard NSK formulation assumes density-dependent transport coefficients and omits non-local corrections that become crucial when the interfacial thickness is small – a common situation in nanoscale evaporation and droplet spreading (Anderson *et al.* 1998). Building on the theoretical framework described above, we propose two significant enhancements to the NSK model. First, we introduce a correction term for intermolecular transfer in the momentum equation from higher-order corrections to the momentum balance formulation developed by Struchtrup & Frezzotti (2022). This modification enables more precise characterisation of momentum exchange at interfaces. Second, we implement density-gradient-dependent transport coefficients – specifically thermal conductivity and viscosity – following the approaches established by Bedeaux, Johannessen & Røsjorde (2003) and Johannessen & Bedeaux (2004). This implementation better accounts for the influence of microscopic fluid structure on transport phenomena within interfacial regions. Indeed, the sudden density change leads to interfacial resistances that are not captured in the classical Korteweg-type models. Thus, in this study, we develop a modified NSK formulation referred to as the augmented Navier–Stokes–Korteweg (ANSK) model for the remainder of the paper, which specifically addresses the limitations of conventional models when applied to nanoscale interfaces, where interfacial thickness and non-local effects become particularly significant. Further, the effectiveness of the ANSK model is assessed by studying three fundamental problems: Couette flow, pure heat conduction and evaporation from a planar surface. Our results demonstrate the gradient-dependent coefficients effectively increase resistance only in the interface. The coefficients in this phenomenological approach are fitted by comparison with solutions of the Enskog–Vlasov (EV) equation (Struchtrup & Frezzotti 2022) for Couette flow. Application of the fitted equations to heat and mass transfer problems yields excellent agreement to EV simulations – a kinetic theory based approach known

https://doi.org/10.1017/jfm.2026.11278 Published online by Cambridge University Press

for its accuracy but high computational cost (Frezzotti & Sgarra 1993; Wu, Zhang & Reese 2015). Additionally, we validate the ANSK model by comparing it with molecular dynamics (MD) simulations for the one-dimensional non-evaporative heat conduction case, and observe excellent agreement in both density and temperature profiles. Thus, our ANSK model offers a balanced framework that combines thermodynamic consistency, computational efficiency and improved fidelity for nanoscale transport processes in dense fluids. The structure of the remainder of the paper is as follows: § 2 presents the conservation laws and their corresponding closure relations. In § 3, the ANSK model is introduced. Section 4 is dedicated to the presentation and analysis of three benchmark problems. Finally, concluding remarks are provided in § 5.

2. Conservation laws from the Enskog–Vlasov equation

We begin with the conservation laws for mass, momentum and energy derived from the EV equation (Sobrino 1967; Grmela 1971; Struchtrup & Frezzotti 2022). Let ρ, $\boldsymbol{v}$, θ, $\boldsymbol{\sigma}$ and $\boldsymbol{q}$ respectively denote mass density, velocity, temperature (in energy units), trace-free kinetic stress tensor and kinetic heat flux. The conservation equations read

$$\frac{\mathrm{D}\rho}{\mathrm{D}t} + \rho\boldsymbol{\nabla}\cdot\boldsymbol{v} = 0, \quad \rho\frac{\mathrm{D}\boldsymbol{v}}{\mathrm{D}t} + \boldsymbol{\nabla}(\rho\theta) + \boldsymbol{\nabla}\cdot\boldsymbol{\sigma} - \rho\boldsymbol{\mathcal{F}} = \boldsymbol{\Upsilon}^1, \tag{2.1a}$$

$$\frac{3}{2}\rho\frac{\mathrm{D}\theta}{\mathrm{D}t} + \rho\theta\boldsymbol{\nabla}\cdot\boldsymbol{v} + \boldsymbol{\sigma}:\boldsymbol{\nabla}\boldsymbol{v} + \boldsymbol{\nabla}\cdot\boldsymbol{q} = \Upsilon^2. \tag{2.1b}$$

The term $\boldsymbol{\mathcal{F}}$, represents the Vlasov force arising from long-range intermolecular interactions (Vlasov 1961), while the transfer terms $\boldsymbol{\Upsilon}^1$, Υ^2 account for the short-range collisional contributions due to finite-size particle effects and local spatial correlations, as described by the Enskog collision operator (Grmela 1971).

The Vlasov force can be expressed as the divergence of the Korteweg stress tensor ($\boldsymbol{\tau}^K$) as $\rho\boldsymbol{\mathcal{F}} = -\boldsymbol{\nabla}\cdot\boldsymbol{\tau}^K$, where $\boldsymbol{\tau}^K$ is given by

$$\boldsymbol{\tau}^K = -\frac{2\pi a^3}{3}\frac{\phi_a}{m}\chi_1\rho^2\,\boldsymbol{I} - \frac{2\pi a^5}{15}\frac{\phi_a}{m}\chi_3\left[\left(\rho\nabla^2\rho + \frac{1}{2}|\boldsymbol{\nabla}\rho|^2\right)\boldsymbol{I} - \boldsymbol{\nabla}\rho\otimes\boldsymbol{\nabla}\rho\right]. \tag{2.2}$$

Here, $\boldsymbol{I}$ is the identity tensor, $\phi_a > 0$ characterizes the strength of the attractive part of the Sutherland potential (Sutherland 1893) and has the same dimensions as temperature, χ_1, χ_3 are the Korteweg coefficients and a, m are the diameter and mass of the particle respectively.

2.1. *Transfer terms from the Enskog collision operator*

To close the system in (2.1), constitutive relations and transfer terms must be expressed in terms of known variables. Following the equilibrium formulation of Wang *et al.* (2020), the momentum transfer term is modelled as

$$\boldsymbol{\Upsilon}^1 = -\frac{2\pi a^3}{3m}\boldsymbol{\nabla}(\rho^2\theta Y)\underbrace{-\frac{4\pi a^3}{15m}\boldsymbol{\nabla}\cdot(\rho Y\boldsymbol{\sigma}) + \boldsymbol{\nabla}\cdot\boldsymbol{\Phi}^{(4)}}, \tag{2.3}$$

where the last two terms above the underbrace have been modelled following Struchtrup & Frezzotti (2022), who take into account the non-equilibrium effects. Here

$$\boldsymbol{\Phi}^{(4)} = \frac{4\sqrt{\pi}a^4}{15m}\left[\boldsymbol{I}\rho^2 Y\sqrt{\theta}(\boldsymbol{\nabla}\cdot\boldsymbol{v}) + \rho^2 Y\sqrt{\theta}\boldsymbol{\nabla}\boldsymbol{v} + \rho^2 Y\sqrt{\theta}(\boldsymbol{\nabla}\boldsymbol{v})^{\mathsf{T}}\right], \tag{2.4}$$

https://doi.org/10.1017/jfm.2026.11278 Published online by Cambridge University Press

whose divergence is the second-order symmetric derivative of velocity – fourth-order correction term in a, following Struchtrup & Frezzotti (2022). The effect of this term considered in the ANSK model shall be discussed in detail in sections to follow.

In a similar manner the energy transfer term following the equilibrium formulation of Wang *et al.* (2020) is modelled as

$$\Upsilon^2 = -\frac{2\pi}{3}\frac{a^3}{m}\rho^2\theta Y(\boldsymbol{\nabla}\cdot\boldsymbol{v}). \tag{2.5}$$

Here, $Y(\rho)$ is the pair correlation function at contact, given by Carnahan & Starling (1969) as

$$Y = \frac{1}{2}\frac{2-\eta}{(1-\eta)^3}, \quad \text{where } \eta = \frac{\pi a^3\rho}{6m} \text{ is the fluid reduced density.} \tag{2.6}$$

Second law of thermodynamics: Assuming entropy depends only on ρ and θ, we postulate the following functional form for the entropy:

$$\varsigma(\rho,\theta) = \frac{3}{2}\ln\theta - \ln\rho - g(\rho), \quad g(\rho) = \frac{2}{3}\frac{\pi a^3}{m}\int Y(\rho)\,\mathrm{d}\rho. \tag{2.7}$$

Using the Gibbs relation and substituting from the conservation laws, the entropy balance gives

$$\rho\frac{\mathrm{D}\varsigma}{\mathrm{D}t} + \boldsymbol{\nabla}\cdot\left(\frac{\boldsymbol{q}}{\theta}\right) = -\frac{1}{\theta}\boldsymbol{\sigma}:\boldsymbol{\nabla}\boldsymbol{v} - \frac{1}{\theta^2}\boldsymbol{q}\cdot\boldsymbol{\nabla}\theta = \Sigma. \tag{2.8}$$

Entropy production is non-negative when the following constitutive relations hold:

$$\boldsymbol{\sigma} = -\mu\left(\boldsymbol{\nabla}\boldsymbol{v} + (\boldsymbol{\nabla}\boldsymbol{v})^{\mathsf{T}}\right) + \frac{2}{3}\mu\,(\boldsymbol{\nabla}\cdot\boldsymbol{v})\,\boldsymbol{I}, \quad \boldsymbol{q} = -\lambda\boldsymbol{\nabla}\theta, \tag{2.9}$$

where $\mu > 0$, $\lambda > 0$ are the shear viscosity and thermal conductivity, respectively. Thus, entropy production $\Sigma \geqslant 0$ is guaranteed, proving the second law of thermodynamics, and the entropy flux is identified as $\boldsymbol{\Psi} = \boldsymbol{q}/\theta$. Together, the conservation laws (2.1), and constitutive relations (2.9) form a closed NSK-type system derived from the EV framework.

3. Augmented Navier–Stokes–Korteweg model

The conservation laws for mass, momentum and energy in conservative form are given by

$$\frac{\partial\rho}{\partial t} + \boldsymbol{\nabla}\cdot(\rho\boldsymbol{v}) = 0, \quad \rho\frac{\mathrm{D}\boldsymbol{v}}{\mathrm{D}t} + \boldsymbol{\nabla}\cdot\boldsymbol{\Pi} = \boldsymbol{0}, \quad \rho\frac{\mathrm{D}}{\mathrm{D}t}\left(\frac{3}{2}\theta + \frac{1}{2}|\boldsymbol{v}|^2 + \varepsilon_K\right) + \boldsymbol{\nabla}\cdot\boldsymbol{\mathcal{J}} = 0, \tag{3.1}$$

where the total momentum and energy flux are defined as

$$\boldsymbol{\Pi} = \left[\rho\theta + \frac{2\pi a^3}{3m}\rho^2\theta Y\right]\boldsymbol{I} + \left(1 + \frac{4\pi a^3}{15m}\rho Y\right)\boldsymbol{\sigma} + \boldsymbol{\tau}^K - \boldsymbol{\Phi}^{(4)}, \tag{3.2}$$

$$\boldsymbol{\mathcal{J}} = \boldsymbol{q} + \boldsymbol{q}^K + \left(\rho\theta\boldsymbol{I} + \boldsymbol{\sigma} + \boldsymbol{\tau}^K\right)\cdot\boldsymbol{v} + \underbrace{\frac{2\pi}{3}\frac{a^3}{m}\rho Y\left(\rho\theta\boldsymbol{v} + \frac{2}{5}\boldsymbol{\sigma}\cdot\boldsymbol{v}\right)}, \tag{3.3}$$

where the terms within the brace in (3.3) have been obtained following the formulation as modelled in Struchtrup & Frezzotti (2022). The potential energy due to the attractive forces (Anderson *et al.* 1998) and the additional energy flux due to non-local effects (Giovangigli

https://doi.org/10.1017/jfm.2026.11278 Published online by Cambridge University Press

2020) are

$$\varepsilon_K = -\frac{2\pi a^3}{3m}\chi_1\phi_a\rho + \frac{\pi a^5}{15m}\chi_3\phi_a\frac{1}{\rho}|\nabla\rho|^2, \quad \boldsymbol{q}^K = \frac{2\pi a^5}{15m}\chi_3\phi_a\rho(\nabla\rho)(\nabla\cdot\boldsymbol{v}). \tag{3.4}$$

To incorporate interfacial and non-equilibrium effects, the transport coefficients – thermal conductivity λ and viscosity μ – are modified to depend on both the local density and its gradient. Such dependencies become significant near phase interfaces, as discussed in Bedeaux *et al.* (2003) and Johannessen & Bedeaux (2004). The expressions for λ and μ are given by

$$\lambda(\rho, |\nabla\rho|) = \frac{15}{4}\frac{\rho\theta\left(1+\frac{2\pi}{5}\frac{a^3}{m}\rho Y\right)^2}{\frac{16}{5}\frac{\rho}{m}\sqrt{\pi\theta}a^2 Y\underbrace{\left[1+\alpha\left(\frac{a}{\rho}|\nabla\rho|\right)^2\right]^2}} + \frac{2}{3}\frac{a^4\sqrt{\pi\theta}}{m}\rho^2 Y, \tag{3.5}$$

$$\mu(\rho, |\nabla\rho|) = \frac{\rho\theta\left(1+\frac{4\pi}{15}\frac{a^3}{m}\rho Y\right)^2}{\frac{16}{5}\frac{\rho}{m}\sqrt{\pi\theta}a^2 Y\underbrace{\left[1+\alpha\left(\frac{a}{\rho}|\nabla\rho|\right)^2\right]^2}} + \frac{4}{15}\frac{a^4\sqrt{\pi\theta}}{m}\rho^2 Y, \tag{3.6}$$

where the coefficient α is a temperature-dependent parameter, detailed in later sections. Interfacial modifications arising from density gradients are highlighted via the underbrace, marking non-equilibrium contributions in the interfacial region.

The ANSK model thus consists of the conservation laws (3.1), constitutive relations (2.9) and modified transport coefficients (3.5)–(3.6), all formulated to satisfy the second law of thermodynamics by ensuring non-negative entropy production. A system that meets this criterion is referred to as thermodynamically consistent.

The requirements on the modified transport coefficients (3.5)–(3.6) are (i) recovery of the correct bulk liquid and vapour transport coefficients, and (ii) reduced transport across the interfacial region, thereby reproducing the principal behaviour of the original EV equation. The adopted functional form satisfies both criteria. While alternative forms could be considered, all admissible choices lead to similar transport-coefficient profiles, characterised by systematically lower values within the interfacial zone.

Phase transition in equilibrium: in equilibrium, the momentum balance equation, the second equation in (3.1), yields the thermal equation of state

$$p(\rho,\theta) = \rho\theta\left(1+\frac{2\pi}{3}\rho Y\right) - \frac{2\pi}{3}\chi_1\rho^2, \tag{3.7}$$

which describes pressure as a non-monotonic function. This behaviour is analogous to the van der Waals equation of state and permits phase separation, as discussed in Struchtrup (2024). Introducing the specific volume $v = 1/\rho$, the critical point is determined from the conditions

$$\left.\frac{\partial p}{\partial v}\right|_{\theta,crit} = 0 \quad \text{and} \quad \left.\frac{\partial^2 p}{\partial v^2}\right|_{\theta,crit} = 0, \tag{3.8}$$

which yield the critical temperature, pressure and volume as $\theta_{critical} = 0.7546$, $p_{critical} = 0.06748$ and $v_{critical} = 4.014$, respectively.

https://doi.org/10.1017/jfm.2026.11278 Published online by Cambridge University Press

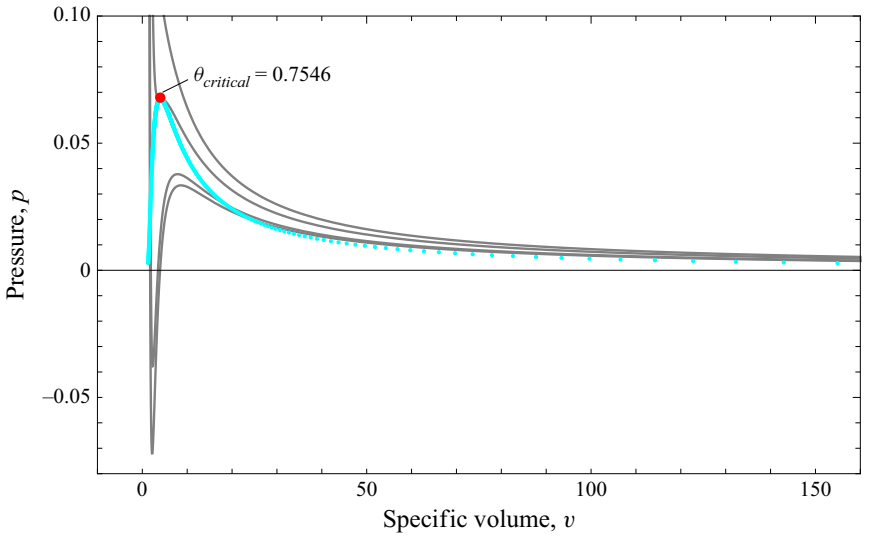


Figure 1. The saturation curve is shown in cyan, with grey lines depicting isotherms at $\theta = 0.85$, 0.75, 0.63, 0.60, arranged from top to bottom in the p–v diagram. The critical point is indicated by a red marker.

Maxwell's equal area rule (Struchtrup 2024) is applied to determine the conditions for phase coexistence below the critical temperature. The rule is expressed as

$$\int_{v_l}^{v_v} p(\theta, v)\,\mathrm{d}v = p_{sat}(v_v - v_l), \tag{3.9}$$

and is evaluated over a range of subcritical temperatures to generate a collection of data points for the saturation pressure $p_{sat}(\theta)$, along with the corresponding specific volumes of the liquid and vapour phases, given by $v_l(\theta) = 1/\rho_l(\theta)$ and $v_v(\theta) = 1/\rho_v(\theta)$, respectively. Here, $\rho_l(\theta) \equiv \rho_l^{sat}(\theta)$ and $\rho_v(\theta) \equiv \rho_v^{sat}(\theta)$ represent the saturated densities of the liquid and vapour phases, respectively.

These results are illustrated in figure 1, which displays a p–v diagram. The saturation curve for the liquid and vapour phases is plotted in cyan, and the isothermal pressure curves $p(\theta, v)$, obtained from (3.7), are shown in grey. The isotherms for temperatures below the critical point clearly exhibit the familiar non-monotonic behaviour that signals the presence of a phase transition.

4. Application of NSK model to three benchmark problems

4.1. *Two-phase isothermal Couette flow*

To validate the ANSK model, we simulate steady, isothermal Couette flow across a liquid–vapour interface and compare results with direct simulation Monte Carlo (DSMC) benchmarks (Rah & Eu 2001; Frezzotti *et al.* 2012). For the physical set-up, we define a coordinate system where the interface normal is aligned with the x-axis. The liquid phase is located in the region $\Omega = \{(x, y, z) \in \mathbb{R}^3 : 0 \leqslant x < x_l\}$, where x_l represents both the upper spatial limit of the liquid region and its nominal thickness. The vapour phase occupies the region to the right of this interface. Flow is unidirectional parallel to the liquid–vapour interface with $\boldsymbol{v}(x) = (0, v_y(x), 0)$, where $v_y(0) = 0$ and $\mathrm{d}v_y/\mathrm{d}x \to const$ as $x \to L$. The incompressible and steady flow satisfies $\boldsymbol{\nabla} \cdot \boldsymbol{v} = 0$, so the governing variables reduce to $\{\rho(x), v_y(x), \sigma_{xy}(x)\}$.

https://doi.org/10.1017/jfm.2026.11278 Published online by Cambridge University Press

All variables are non-dimensionalised by setting $a = m = \phi_a = 1$. Accordingly, length x is scaled by the particle diameter a, density ρ by m/a^3, velocity v by the square root of the potential strength ϕ_a, i.e. $\sqrt{\phi_a}$, and temperature θ by the potential strength ϕ_a. All equations and results that follow are presented in this dimensionless form. The ANSK model reduces to

$$\frac{\mathrm{d}}{\mathrm{d}x}\left\{\left[1+\frac{4\pi}{15}\rho Y\right]\sigma_{xy}-\frac{4\sqrt{\pi}}{15}\rho^2 Y\sqrt{\theta}\frac{\mathrm{d}v_y}{\mathrm{d}x}\right\}=0, \quad \mu\frac{\mathrm{d}v_y}{\mathrm{d}x}+\sigma_{xy}=0. \tag{4.1}$$

The Korteweg coefficients are specified as $\chi_1 = 2$ and χ_3 as a temperature-dependent function defined as $\chi_3(\theta) = c_0 + c_1\theta + c_2\theta^2 + c_3\theta^3$, expressed as a function of θ (for details refer to Bhattacharjee *et al.* 2024*b*). Here, $c_0 = -2.25557$, $c_1 = 18.2905$, $c_2 = -25.0087$ and $c_3 = 18.1759$. Equations (4.1) are discretised using midpoint schemes (Ascher & Petzold 1998), with a uniform mesh in $x \in [0, L]$, with $L = 50$.

In our simulations, we use $n = 1250$ grid points across the domain, which corresponds to 25 grid points per molecular diameter, since the molecular diameter a is set to unity in the non-dimensionalisation.

Boundary conditions: $v_y(0) = 0, \quad \sigma_{xy}\big|_{x=L} = \text{assigned constant}, \quad \mathrm{d}\sigma_{xy}/\mathrm{d}x\big|_{x=0,L} = 0.$

Density- and gradient-dependent coefficients use equilibrium values from (3.1), evaluated as in Frezzotti, Gibelli & Lorenzani (2005), Struchtrup & Frezzotti (2022) and Bhattacharjee *et al.* (2024*b*). The resulting system of linear equations is solved numerically using MATLAB®. The parameter α is varied with the dimensionless temperature θ by fitting it to match the EV equation solutions for the Couette flow problem, following Struchtrup & Frezzotti (2022).

4.1.1. *Analysis of results of the two-phase Couette flow*

Figure 2 presents the velocity profiles $v_y(x)$ for dimensionless temperatures $\theta = 0.55, 0.60$ and 0.65, along with the shear stress $\sigma_{xy}(x)$ at $\theta = 0.65$, compared against EV-DSMC data (black diamonds). The ANSK model (black solid line) shows excellent agreement with DSMC results, reflecting improved interface resistance from the temperature-dependent fitting of α in the modified NSK framework. In contrast, model 1 ($\alpha = 0$), which corresponds to the conventional NSK formulation, fails to resolve the sharp interfacial gradients observed at temperatures far from the critical point (red dashed line). Its performance improves as θ approaches the critical point, where the interface becomes inherently smoother and thicker.

Although the fitted value of $\alpha = 1.925$ at $\theta = 0.65$ is markedly above zero, its effect on the transport coefficients is minimal due to the small density gradients near the critical point. The underbraced gradient-dependent correction term in (3.5) and (3.6) becomes negligible when $|\nabla\rho|$ is small, even if α is large. This explains why both the ANSK model and model 1 produce similar shear velocity profiles at $\theta = 0.65$, despite having different values of α. This observation is further supported by the density gradient profiles plotted at various temperatures ($\theta = 0.45, 0.55, 0.65, 0.75$), shown in figure 3, which demonstrate a clear decrease in $|\nabla\rho|$ as θ approaches the critical value.

Model 2, which omits the fourth-order correction term in a, $\boldsymbol{\Phi}^{(4)}$, results in notable discrepancies in both velocity and stress fields (blue dot-dashed line), underscoring the importance of this term.

The shear stress is largely independent of α, depending instead on the higher-order correction. However, the inclusion of α in the transport coefficients is essential for capturing sharp interface transitions at subcritical temperatures. To determine a suitable temperature-dependent form of α, Couette flow simulations are conducted over a range of

https://doi.org/10.1017/jfm.2026.11278 Published online by Cambridge University Press

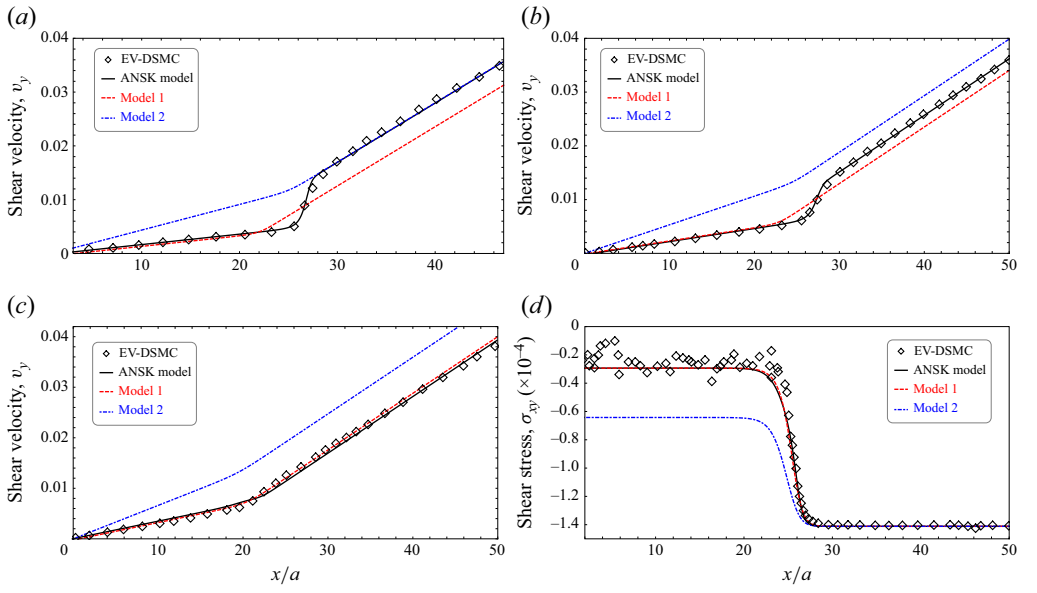


Figure 2. Two-phase Couette flow: comparison of EV-DSMC (black diamonds), ANSK model (black solid line), model 1 (red dashed line) and model 2 (blue dot-dashed line). (*a*) Velocity profiles for $\theta = 0.55$ (*b*) Velocity profiles for $\theta = 0.60$ (*c*) Velocity profiles for $\theta = 0.65$ (top row and bottom left); shear stress at $\theta = 0.60$ (bottom right).

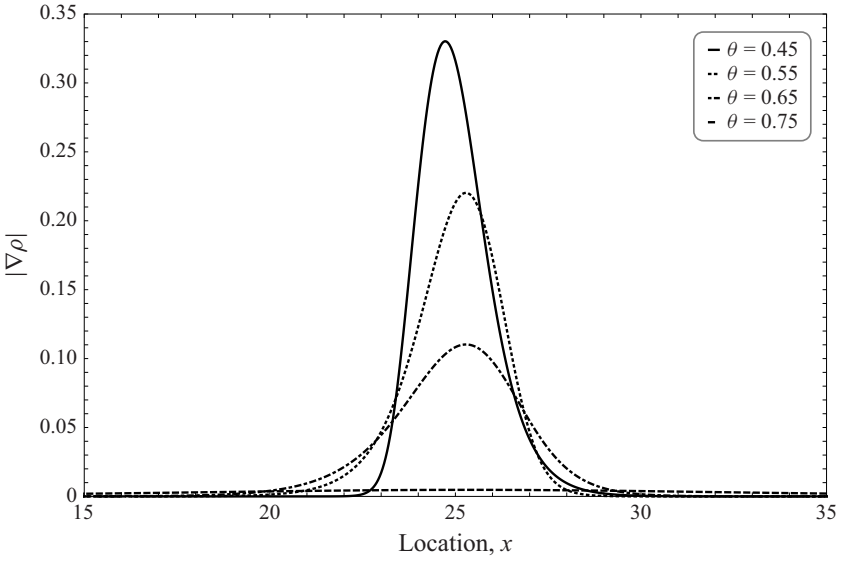


Figure 3. Profiles of the density gradient $|\nabla\rho(x)|$ across the liquid–vapour interface for different dimensionless temperatures $\theta = 0.45, 0.55, 0.65, 0.75$.

θ. A fitting procedure is then employed to match these results with solutions of the EV equation, following the approach outlined by Struchtrup & Frezzotti (2022). This yields the following empirical relation for α as a function of temperature

$$\alpha(\theta) = 9.5\theta - 4.25, \quad 0.45 < \theta < 0.7546. \tag{4.2}$$

This fitted relation is then used in all subsequent analysis.

https://doi.org/10.1017/jfm.2026.11278 Published online by Cambridge University Press

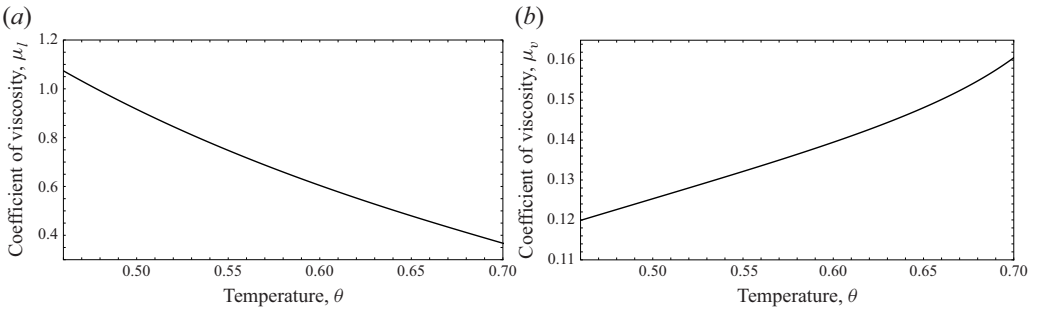


Figure 4. Profiles of the coefficient of viscosity for liquid μ_l, and vapour μ_v versus dimensionless temperature θ.

4.2. *Transport-coefficient properties*

To examine whether the viscosity in the bulk region captures the characteristic temperature-dependent behaviour observed in real fluids, we analyse the variation of viscosity in both the saturated liquid and vapour phases over a range of subcritical temperatures. In real fluids, liquid viscosity (μ_l), generally decreases with increasing temperature, whereas the viscosity of dilute gases (μ_v), shows the opposite trend. In our model, the coefficient of viscosity $\mu(\rho, |\nabla\rho|)$ depends on both local density and its gradient, as defined in (3.6). To evaluate whether this formulation recovers the expected trends in bulk phases, we utilise saturation data obtained through Maxwell's equal area construction. As shown in the p–v diagram of figure 1, isotherms in the liquid region are nearly vertical near the saturation curve, suggesting that density remains approximately constant along an isotherm. Therefore, the liquid viscosity may be approximated by evaluating μ at the saturated liquid density, i.e. $\mu_l(\theta) \approx \mu(\rho_l^{sat}(\theta), \theta)$. In contrast, the vapour isotherms are nearly horizontal, indicating nearly constant pressure and allowing a similar approximation for the vapour phase, $\mu_v(\theta) \approx \mu(\rho_v^{sat}(\theta), \theta)$.

Following this approach, we compute the viscosities of the liquid and vapour phases at various temperatures using the corresponding saturated densities. The resulting trends, presented in figure 4, clearly show that the liquid viscosity decreases with increasing temperature, while the vapour viscosity increases – thus reproducing the classical behaviour. To further clarify the temperature dependence of the viscosity, we note that, along the saturation line, both temperature and density vary, and hence viscosity cannot be regarded as a function of temperature alone. To isolate the true temperature dependence, we evaluate the viscosity at constant pressure for both liquid and vapour phases. In the bulk region, the viscosity obtained from (3.6) may thus be expressed as a function of pressure and density as

$$\mu(p, \rho) = \sqrt{\frac{p + \dfrac{2\pi}{3}\chi_1\rho^2}{\rho\left(1 + \dfrac{2\pi}{3}\rho Y\right)}}\left\{\frac{\left(1 + \dfrac{4\pi}{15}\dfrac{a^3}{m}\rho Y\right)^2}{\dfrac{16}{5}\dfrac{1}{m}\sqrt{\pi}a^2 Y} + \frac{4}{15}\frac{a^4\sqrt{\pi}}{m}\rho^2 Y\right\}, \tag{4.3}$$

and the corresponding temperature follows from the equation of state (3.7) as

$$\theta(p, \rho) = \frac{p + \dfrac{2\pi}{3}\chi_1\rho^2}{\rho\left(1 + \dfrac{2\pi}{3}\rho Y\right)}. \tag{4.4}$$

https://doi.org/10.1017/jfm.2026.11278 Published online by Cambridge University Press

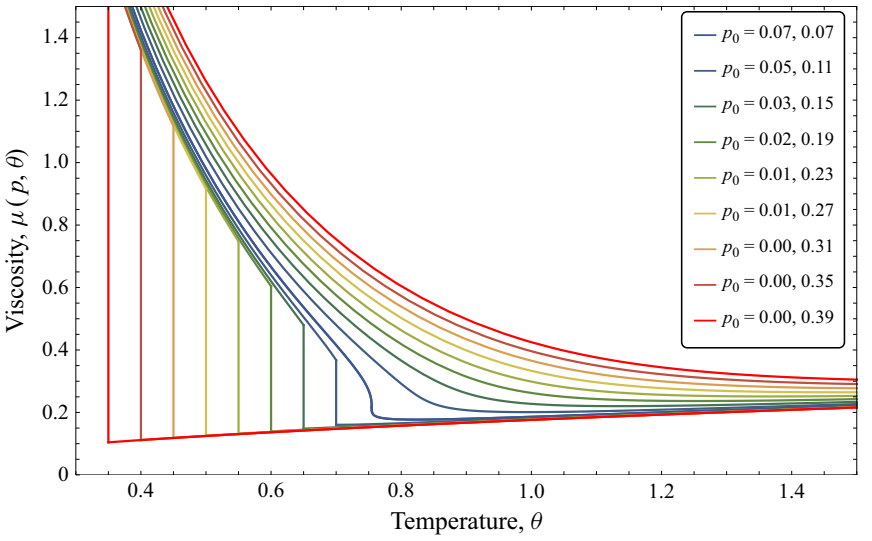


Figure 5. Coefficient of viscosity as a function of temperature at constant pressure. The bottom red solid curve is the ideal gas case where viscosity is independent of pressure.

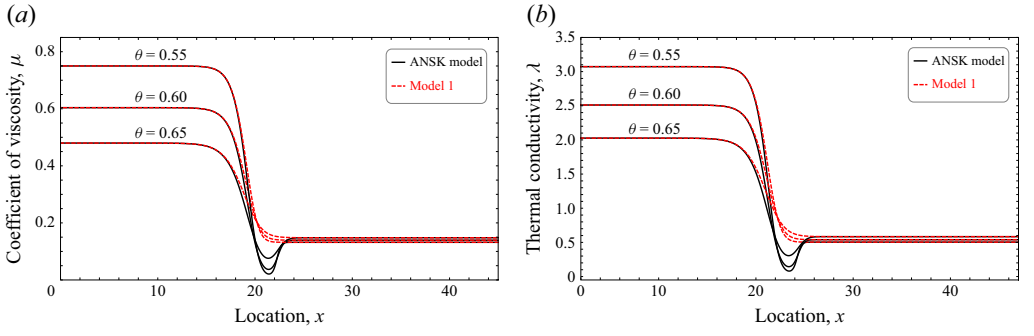


Figure 6. Comparison of coefficient of viscosity (*a*) and thermal conductivity (*b*) computed from ANSK model (black solid line) and model 1 (red dashed line) for $\theta = 0.55$, 0.60 and 0.65.

Figure 5 presents the variation of the viscosity coefficient as a function of temperature for fixed pressures from sub- to supercritical. The curves result from (4.3) and (4.4) by using density as a curve parameter. The plot demonstrates that, at fixed pressure p_0 (say), the viscosity in the liquid phase decreases with increasing temperature, whereas the viscosity in the vapour phase increases with temperature. These results confirm that the viscosity reproduces the correct thermophysical trends when temperature is varied independently of density or pressure effects, consistent with established experimental observations for real fluids.

In the present formulation, the non-local correction appears in the denominator of the transport coefficients. This may seem different from the additive corrections introduced in Bedeaux *et al.* (2003) and Johannessen & Bedeaux (2004). However, it should be noted that their correction applies to the bulk resistances, which are the inverses of the transport coefficients we use in this study. Therefore, the form used here is not fundamentally different but represents the same kind of modification.

To illustrate the impact of this correction, figure 6 shows a comparison between the viscosity profiles and thermal-conductivity profiles predicted by the ANSK model and

https://doi.org/10.1017/jfm.2026.11278 Published online by Cambridge University Press

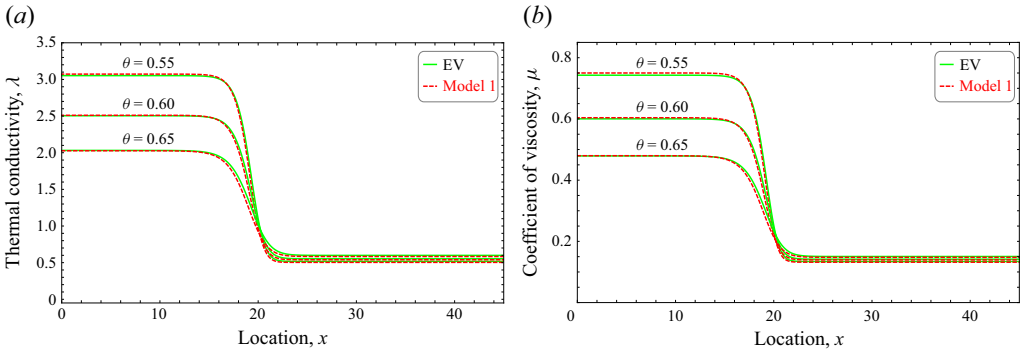


Figure 7. Comparison of coefficient of viscosity (*a*) and thermal conductivity (*b*) computed from EV formulation (green solid line) and NSF framework (red dashed line) for $\theta = 0.55$, 0.60 and 0.65.

model 1 at $\theta = 0.55$, 0.60 and 0.65. The correction introduces a localised dip in the viscosity and thermal conductivity near the interface due to steep density gradients. In addition, figure 7 compares the transport coefficients obtained from the EV formulation (Karkheck & Stell 1981) with those derived from the classical Navier–Stokes–Fourier (NSF) framework (model 1). For $\theta = 0.55$, 0.60 and 0.65, the viscosity and thermal-conductivity profiles predicted by the two formulations overlap across the entire region. While the correction introduced in the transport coefficients of the ANSK model, as illustrated in figure 6, leads to lower values compared with those in the vapour region predicted by model 1, the overall behaviour remains consistent with expected interfacial transport phenomena and does not result in unphysical trends when compared with benchmark models and MD simulations. Since such dips could appear counterintuitive, we next provide a detailed analysis of the Knudsen-number regime and interfacial resistance to demonstrate that the observed trends have a sound physical origin.

4.2.1. *Knudsen effects and interfacial transport resistance*

The NSF equations are typically obtained from the Chapman–Enskog expansion (Struchtrup 2005) in the Knudsen number. This, obviously, requires a small Knudsen number, which is defined as the ratio of the mean free path and the relevant macroscopic length scale.

With the liquid–vapour interface resolved, the natural scale of resolution is the thickness of the interface, which, e.g. can be defined as the distance of locations where in an equilibrium state the local density differs by more than 1 % from the saturation densities in either the liquid or the vapour (99 % thickness $L_{99\,\%}$). Data in table 1 show that the 99 % thickness increases with temperature, and assumes values approximately between 5 and 30 particle diameters.

The mean free path (mfp) of the (saturated) vapour phase can be estimated from the well-known textbook result $L_{HS,v} = 1/\sqrt{2}\pi a^2(\rho/m) = 1/\sqrt{2}\pi\rho_v^{sat}(\theta)$ (Struchtrup 2005; Kremer 2010) (the units are chosen for convenience to be $a = m = 1$), which is a decreasing function of temperature with values in table 1 from approximately 35 at $\theta = 0.45$ to 1 close to the critical temperature.

Small Knudsen numbers imply dominance of local behaviour, while larger Knudsen numbers indicate that non-locality affects transport behaviour. With these values, the vapour mean path is larger than, or comparable to, the interface thickness for a large range of temperatures, and apart from states close to critical, the corresponding Knudsen number is never sufficiently small to warrant a Chapman–Enskog expansion. We must

https://doi.org/10.1017/jfm.2026.11278 Published online by Cambridge University Press

Temperature (θ)	$L_{99\,\%}$	$L_{HS,v}$	$Kn = L_{HS,v}/L_{99\,\%}$
0.45	3.12	34.87	11.17
0.50	3.69	17.53	4.74
0.55	4.49	9.45	2.11
0.60	5.65	5.48	0.97
0.65	7.46	3.38	0.45
0.70	11.22	2.09	0.18
0.75	34.15	1.11	0.03

Table 1. Values of $L_{HS,v}$, the hard-sphere mfp of the saturated vapour phase, 99 % interface thickness $L_{99\,\%}$ and Knudsen number Kn for different dimensionless temperatures θ. The suffix HS, v denotes hard-sphere saturated vapour.

conclude that interface resistance is affected by non-localities that cannot be captured by the NSF equations, which predict a continuous and monotonic change of viscosity and heat conductivity from liquid to vapour.

The typical approach in macroscopic modelling is to consider higher-order moments which allow us to capture non-local transport effects (Torrilhon 2016). This was attempted in Struchtrup & Frezzotti (2022) and Struchtrup *et al.* (2024) with mixed results. It was shown that the NSF framework, when used with transport coefficients obtained via the Chapman–Enskog expansion, severely underestimates interfacial resistance, while models with higher moments overestimate resistance. Thus, it appears rather difficult to develop a physical model – that is, an approximation to the EV equation – that accurately captures the complicated processes within the interface.

We are interested in a NSF model for the bulk phases with a meaningful description of the interface, so that agreement with solutions of the EV equation is sufficiently good. As the comparison of solutions of the original EV-NSF equations and the EV equation shows, the NSF model underestimates interface resistance, so that, e.g. temperature jumps are too small. In the light of the above discussion of Knudsen numbers, this failure of the NSF equations must be attributed to its inability to account for non-local effects.

The proposed correction of the NSF model increases resistance in the interface such that agreement with solutions of the EV equation is acceptable. The corrected model thus mixes physical modelling, i.e. equations and transport coefficients derived from the EV equation, with phenomenological modelling, where transport coefficients are fitted to accurate EV data.

This interpretation is further supported by the fact that the steep density variation across only a few particle diameters in the interface prevents the use of classical continuum arguments based on short mfps. Solutions of the EV equations yield larger temperature jumps and pressure deviations that cannot be described by the NSF equations, unless one corrects the transport coefficients. The observed larger jumps indicate larger interface resistance than expected from NSF, and agreement can be obtained by decreasing viscosity and heat conductivity within the interfacial zone. Thus, the dip observed in figure 6 should not be viewed as unphysical, but rather as the macroscopic representation of the enhanced interfacial resistance captured by kinetic theory.

Additional evidence for this interpretation comes from the behaviour near the critical point. Figure 8 shows the viscosity and thermal-conductivity profiles at $\theta = 0.75$, for which the Knudsen number is $Kn = 0.03$ (see table 1). At this temperature, the mfp becomes much smaller than the interface thickness, indicating that non-local effects are negligible and transport is dominated by local continuum behaviour. Consistent with this expectation,

https://doi.org/10.1017/jfm.2026.11278 Published online by Cambridge University Press

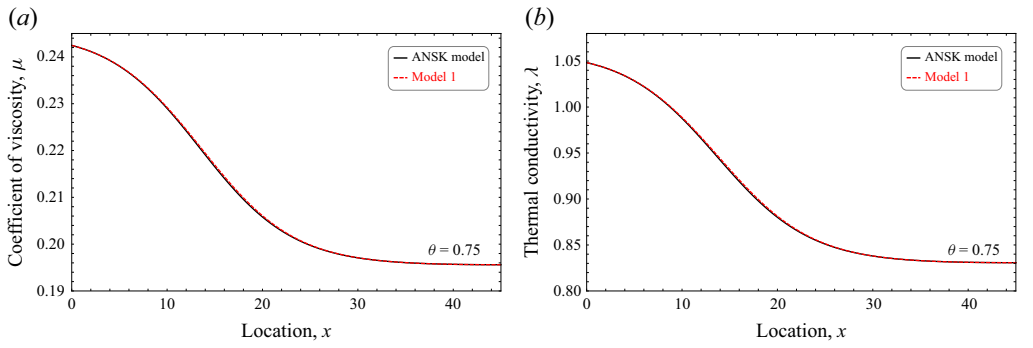


Figure 8. Comparison of coefficient of viscosity (*a*) and thermal conductivity (*b*) computed from ANSK model (black solid line) and model 1 (red dashed line) for $\theta = 0.75$.

the dip observed in figure 6 at lower temperatures disappears entirely, and both transport coefficients vary smoothly and monotonically across the interface. This confirms that the localised reduction in transport coefficients at subcritical temperatures originates from non-local effects rather than from an unphysical artefact of the model. As the Knudsen number decreases toward the critical point, the ANSK model naturally recovers the NSF-like monotonic behaviour, thereby demonstrating that the observed dips are a genuine reflection of enhanced interfacial resistance induced by non-locality.

Overall, the ANSK model incorporating this correction shows excellent agreement with the full EV model and MD simulations, especially in capturing interfacial features. This agreement supports the appropriateness of including gradient-dependent modifications in transport properties for nanoscale systems.

4.3. *One-dimensional steady-state heat transfer without phase change*

Next, we consider steady-state, one-dimensional heat transfer across a liquid–vapour interface without phase change ($J = 0$), where J denotes the total mass flux. The domain $x \in [0, L]$ is discretised with a uniform grid spacing, with the interface located at $x = L_0$. At the liquid boundary ($x = 0$), a constant mass flux J and the temperature θ_l are imposed, while at the vapour boundary ($x = L$), either the vapour temperature θ_v is prescribed or, under adiabatic conditions, the temperature gradient – and thus the heat flux q_V – is set to zero, following Struchtrup *et al.* (2024). The non-zero variables are $\{\rho(x), q_x(x) = q(x)\}$.

Governing equations: Conservation laws for this case now reduce to

$$J = \rho v = 0, \quad \frac{\mathrm{d}}{\mathrm{d}x}\left[\rho\theta + \frac{2\pi}{3}\rho^2\theta Y + \tau_{xx}^K\right] = 0, \quad -\lambda\frac{\mathrm{d}\theta}{\mathrm{d}x} = q_c = \text{constant}, \tag{4.5}$$

where τ_{xx}^K is the one-dimensional Korteweg stress component capturing capillarity effects. We solve (4.5) using a fourth-order finite difference scheme on a uniform grid with $2n$ points, incorporating the boundary conditions and an appropriate initial guess for both density and temperature profiles, as outlined by Struchtrup *et al.* (2024). The resulting $2n + 1$ nonlinear equations are then solved using the `fsolve` command in MATLAB®.

The divergence of the Korteweg stress tensor in (3.1), introduces third-order spatial derivatives in (4.5), which require careful numerical treatment. In our simulations, we use a fourth-order central finite difference scheme on a uniform grid to evaluate all spatial derivatives. This approach provides high accuracy, particularly across the narrow interfacial region where density changes from liquid to vapour over a distance of 10–20 molecular distances. Since the study focuses on steady-state problems, time integration is

https://doi.org/10.1017/jfm.2026.11278 Published online by Cambridge University Press

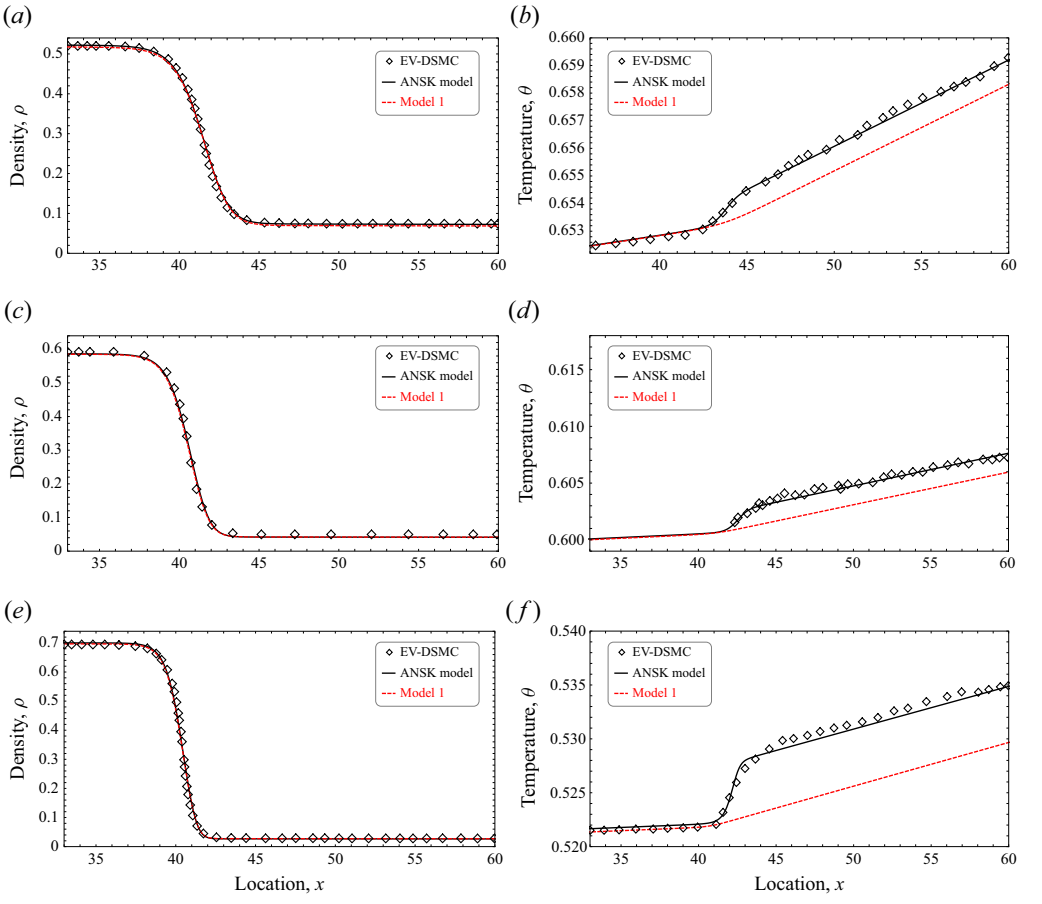


Figure 9. Comparison of density and temperature from the ANSK model (black solid line), EV-DSMC (black diamonds) and model 1 (red dashed line) for three non-evaporative heat transfer cases. Rows: (*a*,*b*) $L = 200$, $\theta_l = 0.65$, $\theta_v = 0.70$, $\alpha = 2.4$, $q_c = -1.90 \times 10^{-4}$; (*c*,*d*) $L = 120$, $\theta_l = 0.60$, $\theta_v = 0.64$, $\alpha = 1.83$, $q_c = -1.55 \times 10^{-4}$; (*e*,*f*) $L = 220$, $\theta_l = 0.52$, $\theta_v = 0.60$, $\alpha = 0.69$, $q_c = -1.99 \times 10^{-4}$; with $L_0 = 40$, $J = 0$.

avoided. Instead, the resulting system of nonlinear algebraic equations is solved using the `fsolve` command in MATLAB®. The grid resolution is chosen such that the interface is resolved with at least 20–30 points. Typical simulations use $n = 1200$–2200 grid points over domains of size $L = 120$–220, depending on the specific problem configuration.

4.3.1. *Results and discussion*

Figure 9 shows density and temperature profiles for different boundary temperatures. The ANSK model (black solid line) shows excellent agreement with EV-DSMC data (black diamonds) (Struchtrup *et al.* 2024), validating the role of the temperature-dependent capillarity coefficient $\chi_3(\theta)$ (Bhattacharjee *et al.* 2024*b*) and gradient-dependent thermal conductivity $\lambda(\rho, \nabla\rho)$ (Bedeaux *et al.* 2003; Johannessen & Bedeaux 2004). Model 1 ($\alpha = 0$), which basically represents the classical NSK equations, agrees well for the density profiles but fails to capture interfacial behaviour and predicts a flat interface for the temperature plots (red dashed line).

The transport coefficients employed in this study are initially derived from the EV equation and subsequently corrected in the interfacial region through comparison with DSMC results based on the Sutherland potential. For more realistic fluids, such as those

https://doi.org/10.1017/jfm.2026.11278 Published online by Cambridge University Press

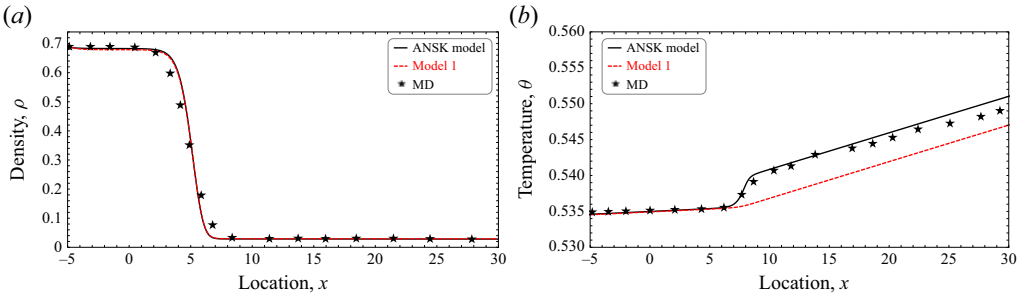


Figure 10. (*a*) Comparison of density and (*b*) temperature profiles from the ANSK model (black solid line), model 1 (red dashed line) and MD simulations (black stars) for non-evaporative heat transfer case. Here, $\theta_l = 0.5348$, $\alpha = 0.52$ and $q_c = -2.55 \times 10^{-4}$.

modelled with the Lennard–Jones potential, these coefficients require adjustment, as done in (Homes *et al.* 2025). To further evaluate the validity of the model, we compare our solution for one-dimensional, non-evaporative heat transfer with MD simulation results reported by Homes *et al.* (2025). In that study, the MD results were transformed for comparison with DSMC data, as detailed in the paper Homes *et al.* (2025), and our results show good agreement with the transformed MD data.

Although the mfp is large in both the vapour phase and the interfacial region, the impact of non-locality on macroscopic transport is fundamentally different in these two settings. In the vapour bulk, the density is nearly uniform and the temperature and velocity profiles remain almost linear, so particles typically traverse their full mfp without encountering strong spatial variations. Under such conditions, the classical NSF constitutive laws remain accurate, as is also observed in standard rarefied-gas flows outside the thin Knudsen boundary layers.

In contrast, the liquid–vapour interface contains very steep density gradients over distances comparable to, or smaller than, the local mfp. This sharply reduces the effective free-travel distance of particles, increases the local collision rate and enhances the influence of the mean-field (Vlasov) forces. As a result, the macroscopic heat and momentum fluxes deviate from the NSF form, and the effective transport coefficients within the interface become smaller than their bulk Enskog values, despite the fact that the underlying microscopic (collisional) coefficients are unchanged.

These observations explain why a change to the classical NSF constitutive laws is needed only in the interfacial region. The strong density gradients there introduce non-local effects that cause the macroscopic fluxes to deviate from the NSF form, even though the underlying Enskog transport coefficients themselves do not change. The gradient-dependent correction offers a practical way to represent this interfacial behaviour within a continuum model, while the vapour phase continues to be well described by the standard NSF relations.

4.4. *Validation against molecular dynamics simulations*

The results depicted by the black solid line in figure 10 represent the solution obtained from the ANSK model, while the red dashed line corresponds to model 1 with $\alpha = 0$, and the black stars denote MD simulation data reported in Homes *et al.* (2025). The ANSK model results shown here are computed at $\theta_l = 0.5348$ (liquid bulk temperature) and $q_c = -2.55 \times 10^{-4}$, with the parameter $\alpha = 0.52$, which is determined phenomenologically in this case to match the MD simulation results. While the ANSK model has been validated against the EV kinetic equation throughout in this study, originally designed for dense

https://doi.org/10.1017/jfm.2026.11278 Published online by Cambridge University Press

hard-sphere fluids, this comparison is intended to further evaluate the model's accuracy by benchmarking it against MD simulations based on realistic interaction potentials.

The comparison shows that both the ANSK model and model 1 provide density profiles that align well with the MD simulation results. However, a clear difference emerges in the temperature predictions. The ANSK model accurately captures the interfacial temperature variation and shows excellent agreement with the MD data. In contrast, model 1 fails to resolve the interfacial structure and instead predicts a nearly flat temperature profile in this region. This discrepancy highlights the limitation of relying on transport coefficients that depend only on the local density. By incorporating density-gradient-dependent transport coefficients – particularly for thermal conductivity – the ANSK model introduces additional thermal resistance near the interface. This allows it to better resolve the temperature gradients observed in the MD simulations. These results underscore the importance of including non-local effects in continuum models when modelling heat transfer at nanoscales.

4.5. *One-dimensional steady state with forced evaporation*

Evaporation strongly influences interfacial heat and mass transport. Following Struchtrup *et al.* (2024), we consider zero heat flux in the vapour bulk (q_V). The non-zero fields for this one-dimensional problem with forced evaporation are $\{\rho(x),\ v_y(x) = v_y,\ \sigma_{xy}(x) = \sigma(x),\ q_x(x) = q(x)\}$.

Governing equations: conservation laws for the case with forced evaporation reduce to

$$\rho v = J = \text{constant}, \quad \frac{\mathrm{d}}{\mathrm{d}x}\left(\rho v_y^2 + \Pi_x\right) = 0, \quad \frac{\mathrm{d}}{\mathrm{d}x}\left[\left(\frac{3}{2}\rho\theta + \frac{1}{2}\rho v_y^2 + \rho\varepsilon_{K,x}\right) v_y + \mathcal{J}_x\right] = 0, \tag{4.6}$$

where Π_x, $\varepsilon_{K,x}$ and $\mathcal{J}_x$ denote the x-components, in the one-dimensional setting, of the total momentum flux tensor, non-local potential energy and energy flux vector as defined above.

Equations (4.6) are solved using the numerical method outlined in (4.3), with boundary conditions at both the left and right boundaries specified based on the EV-DSMC data. These boundary conditions are then used to solve the NSK equations in the bulk, with the resulting solutions serving as initial guess profiles for the equations in (4.6).

4.5.1. *Results and discussion*

Figure 11(*a*,*c*) shows the density and temperature Figure 11(*b*,*d*) profiles for two evaporation cases, with $L_0 = 60$, and $q_V = 0$. Figure 11(*a*,*b*) $\theta_l = 0.60$, $\theta_v = 0.56$, $J = 0.000745$, $\alpha = 1.26$; Figure 11(*c*,*d*) $\theta_l = 0.52$, $\theta_v = 0.48$, $J = 0.00035$, $\alpha = 0.31$. The ANSK model (black solid lines) agrees closely with EV-DSMC results (black diamonds) (Struchtrup *et al.* 2024), for both the density and temperature profile. Model 2 results coincides with the ANSK model showing negligible role of stress gradient in heat transfer problems.

Based on the assigned mass flux $J = \rho v$ and the computed boundary values of density, the evaporative velocities at the domain boundaries in figure 11 indicate that the system operates in a weak evaporation regime. Specifically, the velocities at the liquid boundary range from 4.87×10^{-4} to 1.21×10^{-3}, while on the vapour side, they reach up to 2.80×10^{-2}. Across all cases considered, the maximum evaporative velocity reliably simulated with the present model is 0.1235.

To further examine the applicability range of the ANSK model under increasing non-equilibrium conditions, simulations were performed to examine the temperature jump

https://doi.org/10.1017/jfm.2026.11278 Published online by Cambridge University Press

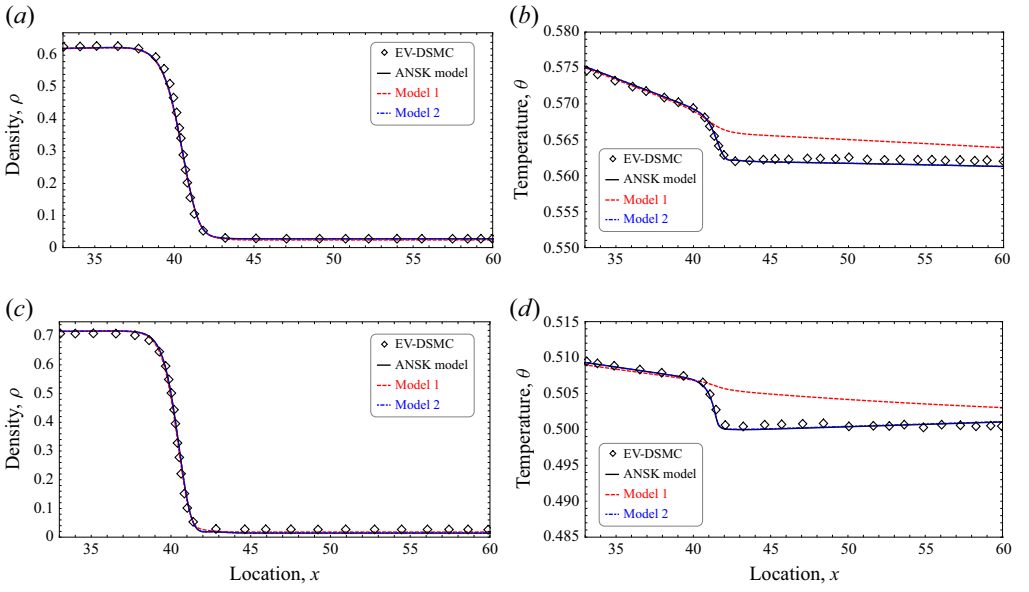


Figure 11. Density and temperature profiles with forced evaporation, comparing the ANSK model, EV-DSMC, model 1 and model 2. (*a–b*) $L = 200$, $\theta_l = 0.60$, $\theta_v = 0.56$, $J = 0.000745$, $\alpha = 1.26$. (*c–d*) $L = 220$, $\theta_l = 0.52$, $\theta_v = 0.48$, $J = 0.00035$, $\alpha = 0.31$. Interface at $L_0 = 60$.

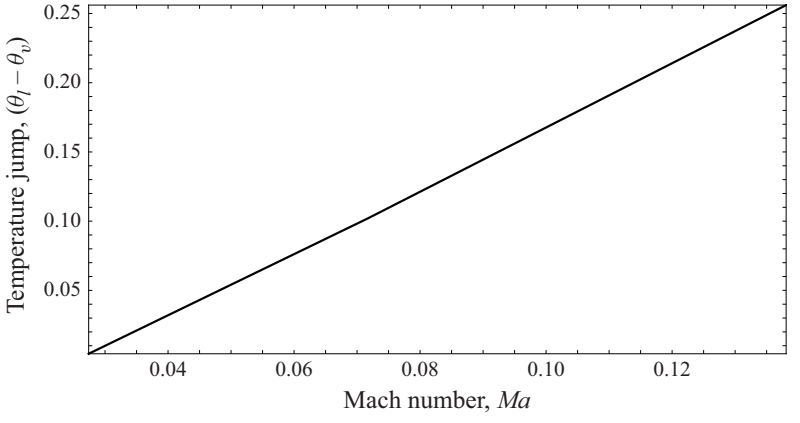


Figure 12. Temperature jump across the interface, defined as $\theta_l - \theta_v$, plotted as a function of the Mach number.

across the interface, defined as $\theta_l - \theta_v$, as a function of the Mach number Ma, given by

$$Ma = \frac{v_0}{\sqrt{\frac{5}{3}\theta_0}}, \tag{4.7}$$

where v_0 denotes the far-field vapour velocity and θ_0 is the reference temperature. As shown in figure 12, the temperature jump increases linearly with Ma, consistent with expectations in the low Mach number regime ($Ma < 0.1$) where the dynamics remains effectively linear. The ANSK model yields converged and physically consistent solutions up to a maximum Mach number of approximately 0.1381. Beyond this point, the numerical method – based on nonlinear root-finding algorithm (MATLAB®'s `fsolve`) – fails to

https://doi.org/10.1017/jfm.2026.11278 Published online by Cambridge University Press

converge. This indicates that the current approach is suitable for weak to moderately strong evaporation regimes, but for higher Mach numbers, more robust numerical schemes such as finite volume methods may be necessary to capture the nonlinearities and ensure convergence.

5. Conclusion

This work presents a thermodynamically consistent extension of the classical NSK model, systematically derived from the EV kinetic equation to accurately capture interfacial transport processes at the nanoscale. While the classical NSK equations assume local equilibrium and density-dependent transport properties (see (3.5) and (3.6)) – assumptions that break down in regions with steep gradients and strong non-equilibrium effects – the proposed model incorporates microscopic physics through a continuum framework. This makes it suitable for simulating dense fluids and multiphase systems where classical formulations fall short. Validation against DSMC for the EV equation across three benchmark problems – two-phase Couette flow, non-evaporative heat conduction and planar evaporation – demonstrates that the ANSK model achieves close agreement with kinetic theory predictions. In particular, the inclusion of a temperature-dependent Korteweg coefficient, density gradient-dependent transport coefficient and a temperature-dependent parameter α in the ANSK model significantly improves the model's accuracy in capturing the interfacial dynamics, without compromising computational efficiency. Moreover, the model adheres to the second law of thermodynamics, as confirmed through a detailed entropy production analysis.

Overall, this study bridges the gap between computationally expensive kinetic theory models and continuum-based approaches, offering a robust framework for applications in nanoscale thermal management, phase-change heat transfer and microfluidic systems.

Despite its strengths, the ANSK model is inherently limited by its five-moment formulation, which includes only mass, momentum and energy conservation. The absence of separate evolution equations for stress and heat flux restricts its ability to resolve non-equilibrium phenomena such as Knudsen layers and other non-equilibrium effects. Capturing these effects would require a more detailed description of the distribution function, for example via higher-order moment approximations, which is only accessible through kinetic models or extended moment closures like the regularised 13-moment equations (Struchtrup & Torrilhon 2003; Rana *et al.* 2021).

Future extensions of this work will address several of these limitations. For example, although the spatial domain in our simulations is non-dimensionalised using the molecular diameter a, the model can be scaled to larger physical domains of the order of hundreds or thousands of nanometres. In dense fluids, where the mfp λ remains small, an increase in domain size L leads to a lower Knudsen number $\mathrm{Kn} = \lambda/L$, thereby reinforcing the applicability of continuum assumptions. Accurate resolution of interfacial gradients in such extended domains may require finer grids or adaptive meshing, which we intend to pursue in future work, particularly for applications such as thin-film evaporation and microscale heat transport.

Furthermore, while the model performs well in weak to moderately strong evaporation regimes, it remains to be seen how the model performs in the strong evaporation case. Most importantly, to improve accuracy in capturing effects such as parallel heat flux in Couette flow – where deviations from Fourier's law are observed – more accurate models, as presented in the literature (Struchtrup & Frezzotti 2022), will also be explored. While the present study focuses on one-dimensional configurations, extending the model to more complex geometries – such as sessile droplets or capillary-driven flows – remains an

https://doi.org/10.1017/jfm.2026.11278 Published online by Cambridge University Press

important direction for future research, as these involve additional physical and numerical challenges.

Acknowledgements. H.S. acknowledges support from NSERC (Discovery Grant RGPIN-2022-03188). A.S.R. acknowledges support from SERB, India (MATRICS MTR/2021/000417).

Declaration of interests. The authors declare that they have no known competing financial interests or personal relationships that could have appeared to influence the work reported in this paper.

References

ANDERSON, D.M., MCFADDEN, G.B. & WHEELER, A.A. 1998 Diffuse-interface methods in fluid mechanics. *Annu. Rev. Fluid Mech.* **30** (1), 139–165.

ASCHER, U.M. & PETZOLD, L.R. 1998 *Computer Methods for Ordinary Differential Equations and Differential-Algebraic Equations*. SIAM.

BEDEAUX, D., JOHANNESSEN, E. & RØSJORDE, A. 2003 The nonequilibrium Van Der Waals square gradient model.(i). The model and its numerical solution. *Phys. A Stat. Mech. Appl.* **330** (3-4), 329–353.

BHATTACHARJEE, R., SAINI, S., GUPTA, V.K. & RANA, A.S. 2024*a* Rarefied gas flow past a liquid droplet: interplay between internal and external flows. *J. Fluid Mech.* **980**, A4.

BHATTACHARJEE, R., STRUCHTRUP, H. & SINGH RANA, A. 2024*b* Temperature dependent Korteweg stress coefficient from the Enskog–Vlasov equation. *Phys. Fluids.* **36** (12), 122139.

CARNAHAN, N.F. & STARLING, K.E. 1969 Equation of state for nonattracting rigid spheres. *J. Chem. Phys.* **51** (2), 635–636.

DHAOUADI, F. & DUMBSER, M. 2023 A structure-preserving finite volume scheme for a hyperbolic reformulation of the Navier–Stokes–Korteweg equations. *Mathematics* **11** (4), 876.

DIEHL, D., KREMSER, J., KRÖNER, D. & ROHDE, C. 2016 Numerical solution of Navier–Stokes–Korteweg systems by local discontinuous Galerkin methods in multiple space dimensions. *Appl. Math. Comput.* **272**, 309–335.

DUPONT, V., THOME, J.R. & JACOBI, A.M. 2004 Heat transfer model for evaporation in microchannels. Part II: comparison with the database. *Intl J. Heat Mass Transfer* **47** (14-16), 3387–3401.

FREZZOTTI, A., GIBELLI, L. & LORENZANI, S. 2005 Mean field Kinetic theory description of evaporation of a fluid into vacuum. *Phys. Fluids.* **17** (1), 012102.

FREZZOTTI, A., ROSSI, M., *et al.* 2012 Slip effects at the vapor–liquid boundary. In *RGD28 2012*, pp. 903–910. AIP.

FREZZOTTI, A. & SGARRA, C. 1993 Numerical analysis of a shock-wave solution of the Enskog equation obtained via a Monte Carlo method. *J. Stat. Phys.* **73**, 193–207.

GARCKE, H. & NOVICK-COHEN, A. 2000 A singular limit for a system of degenerate Cahn-Hilliard equations. *Adv. Differ. Equ.* **5** (4-6), 401–434.

GIBBS, J.W. 1878 On the equilibrium of heterogeneous substances. *Am. J. Sci.* **3** (96), 441–458.

GIOVANGIGLI, V. 2020 Kinetic derivation of diffuse-interface fluid models. *Phys. Rev. E.* **102** (1), 012110.

GOMEZ, H., HUGHES, T.J.R., NOGUEIRA, X. & CALO, V.M. 2010 Isogeometric analysis of the isothermal Navier–Stokes–Korteweg equations. *Comput. Methods Appl. Mech. Engng* **199** (25-28), 1828–1840.

GONG, S., HU, Z. & CHENG, P. 2024 A mesoscopic approach for nanoscale evaporation heat transfer characteristics. *Intl J. Heat Mass Transfer* **231**, 125856.

GRMELA, M. 1971 Kinetic equation approach to phase transitions. *J. Stat. Phys.* **3**, 347–364.

HOMES, S., FREZZOTTI, A., NITZKE, I., STRUCHTRUP, H. & VRABEC, J. 2025 Heat and mass transfer across the vapor–liquid interface: a comparison of molecular dynamics and the Enskog–Vlasov kinetic model. *Intl J. Heat Mass Transfer* **242**, 126828.

JOHANNESSEN, E. & BEDEAUX, D. 2004 The nonequilibrium Van Der Waals square gradient model.(iii). Heat and mass transfer coefficients. *Phys. A Stat. Mech. Appl.* **336** (3-4), 252–270.

KARKHECK, J. & STELL, G. 1981 Kinetic mean-field theories. *J. Chem. Phys.* **75** (3), 1475–1487.

KORTEWEG, D.J. 1901 Sur la forme que prennent les équations du mouvements des fluides si l'on tient compte des forces capillaires causées par des variations de densité considérables mais connues et sur la théorie de la capillarité dans l'hypothèse d'une variation continue de la densité. *Arch. Neerl. Sci. Exactes Nat.* **6**, 1–24.

KREMER, G.M. 2010 *An Introduction to the Boltzmann Equation and Transport Processes in Gases*. Springer Science & Business Media.

LIU, J., GOMEZ, H., EVANS, J.A., HUGHES, T.J.R. & LANDIS, C.M. 2013 Functional entropy variables: a new methodology for deriving thermodynamically consistent algorithms for complex fluids, with particular reference to the isothermal Navier–Stokes–Korteweg equations. *J. Comput. Phys.* **248**, 47–86.

https://doi.org/10.1017/jfm.2026.11278 Published online by Cambridge University Press

MARTÍNEZ, A., RAMÍREZ, L., NOGUEIRA, X., KHELLADI, S. & NAVARRINA, F. 2020 A high-order finite volume method with improved isotherms reconstruction for the computation of multiphase flows using the Navier–Stokes–Korteweg equations. *Comput. Math. Appl.* **79** (3), 673–696.

MUKHERJEE, A. 2009 Contribution of thin-film evaporation during flow boiling inside microchannels. *Intl J. Therm. Sci.* **48** (11), 2025–2035.

RAH, K. & EU, B.C. Theory of nonequilibrium liquid–vapor interface: effects of shear flow. *Phys. A Stat. Mech. Appl.* **292** (1-4), 102–128.

RANA, A.S., GUPTA, V.K., SPRITTLES, J.E. & TORRILHON, M. 2021 H-theorem and boundary conditions for the linear R26 equations: application to flow past an evaporating droplet. *J. Fluid Mech.* **924**, A16.

RANA, A.S., LOCKERBY, D.A. & SPRITTLES, J.E. 2019 Lifetime of a nanodroplet: kinetic effects and regime transitions. *Phys. Rev. Lett.* **123** (15), 154501.

SOBRINO DE, L. 1967 On the Kinetic theory of a Van Der Waals gas. *Can. J. Phys.* **45** (2), 363–385.

SOUČEK, O., HEIDA, M. & MÁLEK, J. 2020 On a thermodynamic framework for developing boundary conditions for Korteweg-type fluids. *Intl J. Engng Sci.* **154**, 103316.

STRUCHTRUP, H.2005 *Macroscopic Transport Equations for Rarefied Gas Flows*. Springer.

STRUCHTRUP, H. 2024 *Thermodynamics and Energy Conversion*, Second edn. Springer International Publishing.

STRUCHTRUP, H. & FREZZOTTI, A. 2022 Twenty-six moment equations for the Enskog–Vlasov equation. *J. Fluid Mech.* **940**, A40.

STRUCHTRUP, H., JAHANDIDEH, H., COUTEAU, A. & FREZZOTTI, A. 2024 Heat transfer and evaporation processes from the Enskog-Vlasov equation and its moment equations. *Intl J. Heat Mass Transfer* **223**, 125238.

STRUCHTRUP, H. & TORRILHON, M. 2003 Regularization of Grad's 13 moment equations: derivation and linear analysis. *Phys. Fluids* **15** (9), 2668–2680.

SUTHERLAND, W. 1893 Lii. The viscosity of gases and molecular force. *Lond. Edinb. Dublin Phil. Mag.* **36** (223), 507–531.

TAASSOB, A., BORDBAR, A., KHEIRANDISH, S., ZARNAGHSH, A., KAMALI, R. & RANA, A.S. 2021 A review of rarefied gas flow in irregular micro/nanochannels. *J. Micromech. Microeng.* **31** (11), 113002.

TIAN, L., XU, Y., KUERTEN, J.G.M., VAN DER, V. & JAAP, J.W. 2016 An h-adaptive local discontinuous Galerkin method for the Navier–Stokes–Korteweg equations. *J. Comput. Phys.* **319**, 242–265.

TORRILHON, M. 2016 Modeling nonequilibrium gas flow based on moment equations. *Annu. Rev. Fluid Mech.* **48** (1), 429–458.

VLASOV, A.A. 1961 *Many-Particle Theory and Its Application to Plasma*. Gordon and Breach.

VAN DER, W. & DIEDERIK, J. 1979 The thermodynamic theory of capillarity under the hypothesis of a continuous variation of density. (Translation by J.S. Rowlinson from the dutch original which appeared in the Verhandel. Konink. Akad. Weten. Amsterdam (sect. 1) vol. 1 no. 8 (1893)). *J. Stat. Phys* **20**(2), 200–244.

WANG, P., WU, L., HO, M.T., LI, J., LI, Z.-H. & ZHANG, Y. 2020 The Kinetic Shakhov–Enskog model for non-equilibrium flow of dense gases. *J. Fluid Mech.* **883**, A48.

WU, L., ZHANG, Y. & REESE, J.M. 2015 Fast spectral solution of the generalized Enskog equation for dense gases. *J. Comput. Phys.* **303**, 66–79.

https://doi.org/10.1017/jfm.2026.11278 Published online by Cambridge University Press